Improved resolution for spin-3/2 isotopes in solids via the indirect NMR detection of triple-quantum coherences using the T-HMQC sequence

Racha Bayzou,[1] Julien Trébosc,[1,2] Ivan Hung,[3] Zhehong Gan,[3] Andrew Rankin,[1,2] Olivier Lafon,[1] Jean-Paul Amoureux,[1,4,*]

[1] Univ. Lille, CNRS, Centrale Lille, Univ. Artois, UMR 8181 – UCCS – Unité de Catalyse et Chimie du Solide, 59000 Lille, France.
[2] Univ. Lille, CNRS, INRAE, Centrale Lille, Univ. Artois, FR 2638 – IMEC – Fédération Chevreul, 59000 Lille, France.
[3] National High Magnetic Field Laboratory, 1800 East Paul Dirac Drive, Tallahassee, Florida, 32310 USA.
[4] Bruker Biospin, 34 rue de l'industrie, 67166 Wissembourg, France.

Corresponding author: Jean-Paul Amoureux jean-paul.amoureux@univ-lille.fr

Abstract.

The indirect NMR detection of quadrupolar nuclei in solids under magic-angle spinning (MAS) is possible with the through-space HMQC (heteronuclear multiple-quantum coherence) scheme incorporating the TRAPDOR (transfer of population in double-resonance) dipolar recoupling. This sequence, called T-HMQC, exhibits limited t_1-noise. In this contribution, with the help of numerical simulations of spin dynamics, we show that most of the time, the fastest coherence transfer in the T-HMQC scheme is achieved when TRAPDOR recoupling employs the highest radiofrequency (rf) field compatible with the probe specifications. We also demonstrate how the indirect detection of the triple-quantum (3Q) coherences of spin-3/2 quadrupolar nuclei in solids improves the spectral resolution for these isotopes. The sequence is then called T-HMQC$_3$. We demonstrate the gain in resolution provided by this sequence for the indirect proton detection of ^{35}Cl nuclei in L-histidine·HCl and L-cysteine·HCl, as well as that of ^{23}Na isotope in NaH_2PO_4. These experiments indicate that the gain in resolution depends on the relative values of the chemical and quadrupolar-induced shifts (QIS) for the different spin-3/2 species. In the case of NaH_2PO_4, we show that the transfer efficiency of the T-HMQC$_3$ sequence employing an rf-field of 80 kHz with a MAS frequency of 62.5 kHz reaches 75% of that of the t_1-noise eliminated (TONE) dipolar-mediated HMQC (*D*-HMQC) scheme.

I. Introduction

Spin-3/2 quadrupolar nuclei, such as ^{7}Li, ^{11}B, ^{23}Na, ^{33}S, ^{39}K, ^{35,37}Cl, ^{63,65}Cu and ^{69,71}Ga represent 26% of the NMR-active isotopes [1]. These nuclei possess an electric quadrupole moment, which interacts with the electric field gradient at the nucleus position. This quadrupolar interaction broadens the NMR resonances and hence, decreases the resolution and sensitivity. These nuclei exhibit two satellite transitions (STs) between energy levels +3/2 ↔ +1/2 and -1/2 ↔ -3/2, as well as the central transition (CT) between energy levels +1/2 ↔ -1/2. The CT is only broadened by the second-order term of the quadrupolar interaction, often over several kilohertz, whereas the STs are broadened by both first- and second-order quadrupolar interactions, often over several megahertz. In one-dimensional (1D) NMR spectra, the STs are often too broad and solely the CT is then detected.

It has been shown that the NMR signal of $I = 3/2$ isotopes, such as ^{35}Cl and ^{71}Ga, can be detected indirectly via protons [2–4]. These two-dimensional (2D) ^{1}H-{I} heteronuclear correlation spectra provide information on the proximities between protons and spin-3/2 isotopes. For instance, probing ^{1}H-^{35}Cl proximities can be useful to characterize the structure and the polymorphism of hydrochloride salts, which represent more than 50% of active pharmaceutical ingredients. The ^{1}H detection of spin-3/2 isotopes has been first achieved using the *D*-HMQC (dipolar-mediated heteronuclear multiple-quantum coherence) sequence [2,3], in which the dipolar couplings between protons and spin-3/2 isotopes are reintroduced by the application of ^{1}H symmetry-based recoupling schemes during both the de- and refocusing delays. However, the 2D *D*-HMQC spectra can exhibit significant t_1-noise, which can mask the true cross-peaks and decrease the sensitivity. This t_1-noise can arise from atomic-level motions in

the microsecond timescale, for instance, in hydrate samples, since these motions modify the spin interactions between the defocusing and refocusing delays and hence, alter the signal intensity from scan to scan. In the absence of significant atomic-level motions, the t_1-noise is mostly produced by the random fluctuations of the MAS frequency, ν_R, which lead to defocusing and refocusing delays that are not perfectly rotor-synchronized [4]. This desynchronization results in an imperfect refocusing of the chemical shift anisotropy of protons (^{1}H CSA) since the heteronuclear dipolar recoupling schemes applied to the ^{1}H channel also reintroduce the ^{1}H CSA and are usually non-γ-encoded. As a result, the amplitude of the ^{1}H signal varies from scan to scan, which leads to an imperfect cancellation of the uncorrelated ^{1}H signal by the phase cycling and hence produces t_1-noise. It has been shown that the t_1-noise can be reduced by refocusing the ^{1}H CSA by inserting two simultaneous π-pulses on the ^{1}H and *I* channels in the middle of the defocusing and refocusing delays of the *D*-HMQC scheme. This variant has been termed TONE (t_1-noise eliminated) *D*-HMQC sequence [4]. Note that a better suppression of ^{1}H CSA and the related t_1-noise can be obtained by applying during the defocusing and refocusing delays the $SR6_2^3$ recoupling on the ^{1}H channel and a train of π pulses to the *I* channel [5]. Nevertheless, this sequence is not suitable for the indirect detection of quadrupolar isotopes since the number of pulses applied to the quadrupolar nuclei must be minimized to improve the efficiency. Another way to decrease the t_1-noise is the use of short recycle delays, τ_{RD}, because this noise is proportional to the signal strength and hence proportional to the signal amplitude [6]. However, this method decreases the sensitivity.

More recently, ^{35}Cl nuclei have been indirectly detected via protons by using a through-space HMQC sequence, in which the ^{1}H-^{35}Cl dipolar interactions are reintroduced by applying one long rectangular pulse on the ^{35}Cl channel during the defocusing and refocusing delays [7,8]. This recoupling is similar to that used in TRAPDOR (transfer of population in double-resonance) [7,8] experiments and this sequence, which has originally been introduced for the indirect of ^{14}N nuclei in solids via spin-1/2 nuclei [9–11], has thus been termed T-HMQC. As these long pulses are applied to the indirectly-detected channel, they do not reintroduce the ^{1}H CSA and hence, the 2D T-HMQC spectra exhibit reduced t_1-noise. Nevertheless, to the best of our knowledge, the sensitivity of T-HMQC experiments has not yet been compared to that of *D*-HMQC-TONE.

So far the ^{1}H-{^{35}Cl} T-HMQC sequence has employed a States-TPPI acquisition and two distinct phase cycles of the TRAPDOR pulses to select the coherence orders of ^{35}Cl nuclei during the t_1 evolution period [7]. In the first case, a two-step phase cycle selects the single-quantum (1Q) coherences of CT and STs as well as the triple-quantum (3Q) one, and thus results in three distinct cross-peaks for each ^{35}Cl sites, which complicates the assignment of the spectra. Alternatively, a four-step phase cycle has been proposed to select the double-quantum (2Q) coherences during the t_1 period [7]. The 2Q resonances are broadened by the first-order quadrupolar interaction. The cancellation of this broadening requires STMAS specifications, *i.e.* an adjustment of the magic angle with an accuracy better than 0.002° and fluctuations of the MAS frequency smaller than a few hertz [12]. However, these 2Q coherences exhibit a second-order quadrupolar broadening nine-fold smaller in hertz than that of 1Q-CT, along with a twofold increase in chemical shifts. Therefore, the indirect detection of 2Q coherences may improve the resolution by a factor of 18, on average, with respect to that of 1Q-CT for well-crystallized samples, when the STMAS specifications are met.

In this contribution, we demonstrate with the help of numerical simulations that the optimal rf-field amplitude for the TRAPDOR pulses in the T-HMQC sequence is approximately equal to $\sqrt{0.5\nu_R C_Q}$, where ν_R is the MAS frequency and $C_Q = e^2qQ$ is the quadrupolar coupling constant. Nevertheless, this value generally exceeds the rf power specifications of most MAS probes and hence, usually the maximal rf-field amplitude compatible with the probe specifications must be employed. Furthermore, we also introduce a six-step phase cycle of the T-HMQC experiment, denoted T-HMQC$_3$ hereafter, which solely selects the 3Q coherences of spin-3/2 isotopes during the t_1 period. We demonstrate that this phase cycling can yield an average fourfold improvement of the resolution along the indirect dimension of T-HMQC$_3$ with respect to that observed with *D*-HMQC sequences.

Even if this resolution improvement is lower than that achievable for the indirect detection of 2Q coherences, the indirect detection of 3Q ones has the advantage that it does not require STMAS specifications since the 3Q coherences are not broadened by the first-order quadrupolar interaction. In this article, we demonstrate the proton detection of 3Q coherences of ^{35}Cl nuclei in L-histidine·HCl and L-cysteine·HCl, as well as those of ^{23}Na species of NaH_2PO_4 using T-HMQC$_3$. These experiments show

that the actual resolution improvement depends on the relative chemical and quadrupolar-induced shifts (QIS) of the different species. We show experimentally on NaH_2PO_4 that with an rf-field of 80 kHz and a MAS frequency of 62.5 kHz the transfer efficiency of T-HMQC$_3$ is approximately 75% that of the *D*-HMQC-TONE scheme.

II. Pulse sequences and theory

II.1 Pulse sequences

The ^{1}H-{*I*} T-HMQC, *D*-HMQC and *D*-HMQC-TONE$_2$ pulse sequences are displayed in Fig.**1**. They all consist of a rotor-synchronized spin-echo on the ^{1}H channel, *i.e.* the delay between the centers of the $\pi/2$ and π pulses as well as that between the center of the π pulse and the beginning of the acquisition period, t_2, are equal to an integer multiple of rotor periods, mT_R, where $T_R = 1/\nu_R$.

In the T-HMQC sequence (Fig.**1a**), the ^{1}H-*I* dipolar couplings are reintroduced during the echo delays by applying two long rectangular pulses of identical length, τ_{mix}, and rf-amplitude, ν_1. These long pulses create and reconvert the *I* coherences, which evolve during the indirect evolution period, t_1. The phase cycling of one of these long pulses allows the selection of the coherence order of the *I* isotope during the t_1 period. For $I = 3/2$, a two-step phase cycle selects simultaneously the 1Q and 3Q coherences, whereas a four-step phase cycle selects the 2Q ones [7,8]. We introduce herein a six-step phase cycle to select solely the 3Q coherences. The corresponding experiments are denoted T-HMQC$_p$ hereafter, where p is the coherence order selected. Note that the sole indirect detection of 1Q coherences using T-HMQC would require to select alternatively the +1Q and −1Q coherences during the t_1 period, using a phase cycle with at least five steps as well as an echo/anti-echo acquisition mode. The selection of only one of the two coherence transfer pathways, instead of both ±1 levels for T-HMQC$_1$, reduces the sensitivity by a factor of $\sqrt{2}$. Another possibility for the sole detection of the 1Q-CT is to add two CT-selective π-pulses, one before and one after the t_1 evolution period, in the T-HMQC$_1$ sequence, however this method does not allow the observation of the 1Q-ST coherences.

The ^{1}H-{*I*} *D*-HMQC pulse sequence is displayed in Fig.**1b**. The ^{1}H-*I* dipolar couplings are then recoupled by applying a rotor-synchronized scheme, here $SR4_1^2$ [13], on the ^{1}H channel. We use herein CT-selective $\pi/2$ pulses on the *I* channel to create and reconvert the 1Q-CT coherences during the t_1 period. However, non-selective pulses were also employed for the indirect detection of both 1Q CT and STs [2]. Note that the $SR4_1^2$ recoupling is non-γ-encoded, and that besides the ^{1}H-*I* dipolar coupling, it also reintroduces the ^{1}H CSA. However, the evolution under ^{1}H CSA is theoretically refocused by the π-pulse on ^{1}H channel.

The ^{1}H-{*I*} *D*-HMQC-TONE$_2$ variant is displayed in Fig.**1c** [4]. This sequence derives from that of *D*-HMQC by the simultaneous application of π-pulses on ^{1}H and *I* channels in the middle of the defocusing and refocusing periods to cancel the evolution under ^{1}H CSA, and hence, to reduce the t_1-noise. Furthermore, a flip-back ^{1}H $\pi/2$-pulse at the end of the defocusing period transforms the in-phase ^{1}H magnetization, which has not be transferred to the *I* isotope, into longitudinal magnetization. This flip-back pulse reduces the amplitude of the uncorrelated ^{1}H signal and hence, the t_1-noise.

II.2 Effective Hamiltonians

II.2.1. T-HMQC

We have recently derived the effective TRAPDOR Hamiltonian in the quadrupolar jolting frame for a spin $I = 3/2$ [8]. When the carrier frequency of the TRAPDOR pulse is resonant with a spinning sideband of the *I* nucleus ($\nu_{off} \approx n\nu_R$ with $n \neq 0$) and the amplitude of the rf-field, ν_1, is much lower than the MAS frequency, $\nu_1 \ll \nu_R$, the spin dynamics can be conveniently described in the quadrupolar jolting frame [8,14,15]. The lowest-order term of the effective Hamiltonian involving the ^{1}H-*I* dipolar coupling is then a second-order cross-term between the rf Hamiltonian and the ^{1}H-*I* dipolar interaction, proportional to $\sqrt{\alpha}b_{IS}S_z$, where b_{IS} is the ^{1}H-*I* dipolar coupling constant, S_z is the component of the ^{1}H spin along the *z*-axis and the adiabacity parameter α [16], is given for a spin-3/2 isotope by

$$\alpha = \frac{\nu_1^2}{\nu_R C_Q}. \quad (1)$$

When this lowest-order term is sufficient to describe the evolution of the ^{1}H transverse magnetization under ^{1}H-*I* dipolar coupling, the optimal recoupling time, $\tau_{mix,opt}$, is inversely proportional to b_{IS} and ν_1. Therefore, a high rf-field during TRAPDOR pulses shortens the recoupling time and hence, reduces the losses due to ^{1}H-^{1}H dipolar interactions during the defocusing and refocusing delays. When the TRAPDOR pulse is resonant with the center-band ($\nu_{off} \approx 0$), the second-order cross-terms are opposite for the two satellite transitions and orthogonal to the effective rf Hamiltonian, which decouples the ^{1}H-^{35}Cl dipolar couplings. As the result, the transfer efficiency of the T-HMQC sequence drops for on-resonance irradiation of the *I* nucleus.

We have also shown that the third-order effective Hamiltonian between two rf Hamiltonians and ^{1}H-*I* dipolar coupling, which is proportional to $\alpha b_{IS} S_z$, and hence to ν_1^2, can transform the ^{1}H transverse magnetization into multiple-quantum ^{1}H-*I* coherences involving the 2Q coherences of *I* isotope, when irradiating the midpoint between two consecutive spinning sidebands ($\nu_{off} \approx (n \pm 1/2)\nu_R$). Furthermore, the fourth-order effective Hamiltonian between three rf Hamiltonians and ^{1}H-*I* dipolar coupling, which is proportional to $\alpha^{3/2} b_{IS} S_z$, and hence to ν_1^3, can convert the ^{1}H transverse magnetization into multiple-quantum ^{1}H-*I* coherences involving 1Q-CT, 1Q-ST and 3Q, when $\nu_{off} \approx (n \pm 1/3)\nu_R$. The contributions of these higher order terms are proportional to ν_1^2 and ν_1^3, whereas the second-order term is proportional to ν_1, and hence, they increase for higher rf-field. Furthermore, as TRAPDOR experiments are usually performed under experimental conditions, such that $\alpha \leq 1$ (see section III.2), the amplitudes of the third- and fourth-order terms are smaller than that of the second-order effective Hamiltonian and their contributions increase with the recoupling time.

It must be noted that because of the truncation by the effective rf Hamiltonian, the reintroduced dipolar Hamiltonians during T-HMQC commute among different spin pairs, whereas they do not before this truncation. As a result, the 2D T-HMQC spectra exhibit cross-peaks between ^{1}H and remote *I* nuclei.

II.2.2. *D*-HMQC

In the case of the *D*-HMQC and *D*-HMQC-TONE sequences, the ^{1}H-*I* dipolar couplings are reintroduced during the defocusing and refocusing delays by applying e.g. the $SR4_1^2$ recoupling on the ^{1}H channel. When built from single π-pulses, this scheme requires an rf-field amplitude $\nu_1 = \nu_R/2$. The ^{1}H-*I* dipolar coupling contributes to the first-order average Hamiltonian by the term:

$$\bar{H}_{D,IS}^{(1)} = 2\omega_{D,IS} I_z S_z \tag{2}$$

where

$$\omega_{D,IS} = \kappa b_{IS} \sin^2\left(\beta_{PR}^{D,IS}\right)\cos(2\varphi) \tag{3}$$

with

$$\varphi = \gamma_{PR}^{D,IS} - \omega_R t^0. \tag{4}$$

In the above equations, $\kappa = 0.131$, the Euler angles $\left\{0, \beta_{PR}^{D,IS}, \gamma_{PR}^{D,IS}\right\}$ relate the *I*-*S* vector to the MAS rotor frame, $\omega_R = 2\pi\nu_R$, and t^0 refers to the starting time of the recoupling. The norm of $\bar{H}_{D,IS}^{(1)}$ depends on $\gamma_{PR}^{D,IS}$, and hence the $SR4_1^2$ scheme is non-γ-encoded [17,18]. The Hamiltonian of Eq. 2 commutes among different spin pairs, and hence, the *D*-HMQC and *D*-HMQC-TONE sequences are not affected by dipolar truncation.

II.3 Chemical shift scale and quadrature detection

The chemical shift evolution in Hz is proportional to the coherence order, p. To compare the indirect dimension of T-HMQC$_p$ spectra with different p values, we will use a universal shift ppm scaling:

$$\delta_{pQ} = 10^6 \frac{\nu_{I0} - p\nu_{0,Iref}}{p\nu_{0,Iref}} \tag{5}$$

where ν_{I0} is the resonance frequency and $p\nu_{0,Iref}$ is the resonance frequency of the pQ coherence of the reference compound. This scaling has already been employed for the indirect dimension of the T-HMQC$_2$ sequence [7], and the MQMAS/STMAS spectra. In the latter case, this representation has been termed 'universal ppm scaling', which also allows to have the same 2D sheared representation with

STMAS, 3QMAS, 5QMAS etc [19]. It must be noted that other representations of MQMAS and STMAS spectra are employed but they do not preserve the chemical shift values and hence, they prevent an easy comparison of MQMAS and STMAS spectra [20]. In the following, the T-HMQC$_1$, T-HMQC$_2$ and T-HMQC$_3$ spectra are displayed with the δ_{1Q}, δ_{2Q} and δ_{3Q} shift scales along the indirect dimension, respectively.

The quadrature detection along the indirect dimension of T-HMQC spectra was achieved using the States-TPPI procedure [21] with a phase increment of 90°, 45° and 30° for T-HMQC$_1$, T-HMQC$_2$ and T-HMQC$_3$ experiments, which correspond to an effective rotation of 90° for 1Q, 2Q and 3Q coherences in these sequences. Nevertheless, in T-HMQC$_1$ experiments, the phase increment of 90° results in an effective rotation of 270° = -90° for the 3Q coherences, i.e. a shift of the carrier frequency by $-\nu_{off}$, whereas the 3Q coherences evolve at $3\nu_{off}$. Therefore, the frequency position of 3Q coherences varies with offset as $4\nu_{off}$.

The *D*-HMQC spectra were displayed with δ_{1Q} scale along the indirect dimension and the quadrature detection along this dimension was achieved using States-TPPI procedure with a phase increment of 90°.

II.4 Resolution

As mentioned above, the 1Q-CT and 3Q coherences are not affected by the first-order quadrupolar interaction, unlike the 1Q-ST and 2Q coherences. However, when these latter are indirectly detected, their broadening by the first-order quadrupolar interaction can be refocused by MAS provided the magic angle is carefully adjusted and the spinning frequency is highly stable, i.e. the STMAS specifications are met [12,19,22–24].

Under these conditions, the linewidths of the resonances are dominated by the second-order quadrupolar broadenings, which depend on the type of coherence as shown in Table 1 [25,26]. Moreover, the centers of gravity of the resonances are determined by the sums of the isotropic chemical shift, δ_{iso}, and the QIS, which is the isotropic part of the second-order quadrupolar interaction, which also depends on the type of coherence as shown in Table 1. When the *I* species are subject to the same quadrupolar interactions, the resolution of the 3Q spectrum is improved by a factor 27/7 with respect to the 1Q-CT spectrum. Nevertheless, when the deshielded resonance of the *I* isotope exhibits a larger QIS than the shielded one, the resolution improvement of the 3Q spectrum with respect to the 1Q-CT one is larger than this factor. Conversely, when the deshielded resonance of the *I* isotope exhibits a smaller QIS than the shielded one, the resolution improvement of the 3Q spectrum is lower than 27/7. Furthermore, for 3Q coherences, the negative sign of $\langle H_{Q2}\rangle$ indicates a reversed line-shape with respect to the 1Q-CT spectrum.

Table 1. QIS and anisotropic total linewidth $\langle H_{Q2}\rangle$ expressed in δ_{pQ} scale for the different coherences of spin-3/2 isotope. QIS and $\langle H_{Q2}\rangle$ are given in unit of $(C_Q/\nu_{0I})^2(1 + \eta_Q^2/3)/40$ and $\{(6 + \eta_Q)C_Q/\nu_{0I})\}^2/672$, respectively, where η_Q is the asymmetry parameter of the electric field gradient (efg) tensor. For ^{35}Cl nuclei in L-histidine·HCl and L-cysteine·HCl, for which (C_Q (MHz), η_Q) are equal to (1.95, 0.66) and (4.78, 0.43), these units are equal at 18.8 T ($\nu_{0,35Cl}$ = 78.427 MHz) to 17.7 and 98.6 ppm for QIS, and 41 and 229 ppm for $\langle H_{Q2}\rangle$, respectively.

	1Q-CT	1Q-ST	2Q-ST	3Q
QIS	−1	2	0.5	1
$\langle H_{Q2}\rangle$	1	−8/9	1/18	−7/27

III. Numerical simulations

III.1 Simulation parameters

Numerical simulations were carried out using the SIMPSON software [27] for an isolated ^{1}H-^{35}Cl spin pair without ^{1}H CSA. The powder averaging was performed using 168 $\{\alpha_{MR}, \beta_{MR}\}$ pairs and 11 γ_{MR} Euler angles to relate the molecular and rotor frames. The $\{\alpha_{MR}, \beta_{MR}\}$ pairs were selected according to the REPULSION algorithm [28], whereas the γ_{MR} angle was regularly stepped between 0° and 360°. The dipolar coupling constant was equal to $|b_{1H\text{-}35Cl}|/(2\pi)$ = 580 Hz and the ^{35}Cl C_Q was equal to 1.95 MHz with η_Q = 0.66, i.e. the ^{35}Cl quadrupolar parameters of L-histidine·HCl, except in Fig.**3d**,**e**, where the build-up curves were also simulated for a four-fold lower C_Q value equal to 487.5 kHz and in Fig. **S1a**,**b**, where they were also simulated for a two-fold larger C_Q value equal to 3.90 MHz.

The simulations were carried out at B_0 = 18.8 T with ν_R = 62.5 kHz, except in Fig.3d,e, where they were also performed with ν_R = 15.625 kHz. For all simulations, the t_1 period was null to avoid the evolution of *I* nuclei. The τ_{mix} delays were equal to an integer multiple of rotor periods, mT_R. The pulses on ^{1}H channel were simulated as ideal Dirac ones. The transfer efficiency was normalized with respect to that of a spin-echo made with ideal $\pi/2$ and π Dirac pulses applied to the ^{1}H channel. The coherences 1Q (CT + ST), 1Q-CT and 3Q were selected during the t_1 period. The SIMPSON code is provided in SI.

III.2 Simulated 1Q and 3Q ^{1}H-{*I* = 3/2} T-HMQC transfer efficiencies

Fig.2 displays the ^{1}H-{^{35}Cl} T-HMQC$_1$ efficiency versus the offset in reduced value, ν_{off}/ν_R, for three distinct rf-fields of the TRAPDOR-pulses. For a small rf-amplitude (ν_1 = 10 kHz, Fig.2a), the second-order cross-term between the ^{1}H-^{35}Cl dipolar interaction and the rf-field represents the main contribution to the effective Hamiltonian and the transfer efficiency is maximal at $\nu_{off} \approx n\nu_R$ with $n \neq 0$, i.e. when the TRAPDOR pulse is resonant with a spinning sideband of the *I* nucleus. However, for a larger rf-field, e.g. ν_1 = 20 kHz, a high efficiency is also achieved for other offset values, as seen in Fig.2b, showing that the third- and fourth-order Hamiltonians also contribute to the transfer. When the rf-field is large, e.g. ν_1 = 100 kHz (Fig.2c), the condition $\nu_1 \ll \nu_R$ and hence, the effective Hamiltonians derived in ref. [8] are no longer valid and an efficient coherence transfer is achieved outside $\nu_{off} \approx n\nu_R$, $(n \pm 1/2)\nu_R$ and $(n \pm 1/3)\nu_R$ corresponding to second-, third- and fourth-order Hamiltonians. In particular, for sufficiently long τ_{mix} delays, the offset profile is almost flat, except the on-resonance trough.

Figs.3a and 3c show the offset profile of the T-HMQC sequence selecting 1Q and 3Q coherences during t_1 for three different rf-fields for the TRAPDOR pulses (ν_1 = 20, 50 and 100 kHz). For each rf-field, the recoupling time was optimized, but it must be noted that the $\tau_{mix,opt}$ values were the same for 1Q and 3Q selections. However, the 1Q-ST resonances are subject to the first-order quadrupolar interaction and hence, are difficult to observe. Therefore, the most important comparison is that between the 1Q-CT (Fig.3b) and 3Q (Fig.3c) coherences, which are both only subject to a second-order quadrupolar broadening. For the selected coherences and rf-field range, we observe a significant increase of the efficiency for increasing rf-fields. The signals associated to the 1Q-CT and 3Q coherences have similar efficiencies (ca. 4 %), in agreement with previously reported experimental results (see Fig.18 of ref. [8]). The efficiency for the selection of these coherences is ca. twice smaller than for the selection of the two 1Q-ST coherences.

We also simulated the build-up curves of the T-HMQC$_1$ sequence selecting the 1Q (CT + ST) coherences during the t_1 period for $\nu_{off} = \nu_R$ and the α parameter ranging from 3.2×10^{-3} to 8.2 in Fig.S1 and 3.3×10^{-3} to 0.33 in Fig.3d,e. As seen in Fig.S1, the $\tau_{mix,opt}$ value decreases inversely to the rf-field for $\alpha \leq 0.5$, i.e. ν_1 = 247 kHz for C_Q = 1.95 MHz and ν_1 = 350 kHz for C_Q = 3.90 MHz, and then increases for larger rf-fields. Nevertheless, the ν_1 values corresponding to $\alpha \approx 0.5$ are usually much larger than the maximal rf-field compatible with the rf power probe specifications. Hence, the largest rf-field compatible with the probe specifications must be employed to reduce the recoupling time and hence limit the losses due to ^{1}H-^{1}H dipolar interactions. Furthermore, as seen in Fig.3d,e, the initial slopes of the build-up curves for $\alpha \leq 0.3$ are approximately proportional to $\sqrt{\alpha}$.

IV. Experiments

IV.1. Samples and experimental conditions

L-histidine·HCl, L-cysteine·HCl (denoted histidine and cysteine hereafter) and NaH_2PO_4 crystalline powders were purchased from CortecNet. All experiments were performed on Bruker BioSpin Avance NEO spectrometers with 1.3 mm MAS probes. Those on histidine and cysteine were performed at 18.8 T with a double-resonance ^{1}H/X probe, whereas those on NaH_2PO_4 were carried out at 9.4 T with a triple-resonance ^{1}H/X/Y probe used in double-resonance mode. For all experiments, the MAS speed was regulated at ν_R = 62.5 kHz using a MAS-III pneumatic unit. The ^{1}H rf-field for $\pi/2$ and π pulses was always set to 208 kHz. A pre-saturation consisting of five $\pi/2$ pulses was applied on ^{1}H channel to use recycling delays shorter than five times the longitudinal relaxation time of protons, $T_{1,1H}$. The 2D ^{1}H-{^{35}Cl} and ^{1}H-{^{23}Na} *D*- and T-HMQC spectra were acquired using rotor-synchronized t_1 increments, *i.e.* $\Delta t_1 = T_R$. The quadrature along the indirect dimension of these 2D spectra was achieved using a

States-TPPI procedure [21], and a phase increment of the first pulse on I = ^{23}Na and ^{35}Cl channels of 90° for *D*-HMQC and T-HMQC$_1$, 45° for T-HMQC$_2$ or 30° for T-HMQC$_3$. The 1D spectra were acquired with $t_1 = 0$. The number of scans, *NS*, the number of t_1 increments, N_1, and the total experimental time, T_{exp}, are given in the captions of either Figs.**S3** and **S4** or Figs.**5** and **6**, for histidine and cysteine or NaH_2PO_4, respectively.

Histidine and cysteine. The 1D ^{1}H MAS spectra were acquired by averaging 16 transients separated by a recycle delay of 1s using the DEPTH sequence for probe background suppression (Fig.**S2a**) [29]. We measured $T_{1,1H}$ = 1 and 3 s for histidine and cysteine samples using a saturation-recovery experiment. The sensitivity for the acquisition of the 1D ^{35}Cl spectra was enhanced by (i) irradiating the STs with DFS (double-frequency sweep) [30] to enhance the population difference across the CT and (ii) the acquisition of multiple echoes using quadrupolar CPMG (Carr-Purcell Meiboom-Gill) detection [31]. The 1D CPMG spectra, which are the FT of the sum of the echoes, were simulated using the dmfit software [32]. The DFS pulse lasted 1 ms and employed a maximal rf-field amplitude of 50 kHz. During this pulse, the two rf carrier sidebands were linearly swept from ±180 to ±242.5 kHz in a symmetric manner. The CPMG scheme employed a train of CT-selective π pulses with a length of 3 μs and an rf-field of 50 kHz (as measured on a liquid). Under MAS conditions, the refocusing pulses were repeated with a cycle time of 3 ms and 30 echoes were used for each transient. We acquired the 2D ^{1}H-{^{35}Cl} *D*- and T-HMQC$_p$ spectra with a recovery delay, $\tau_{RD} = T_{1,1H}$. For these experiments, the rf-field of the pulses on ^{35}Cl channel was equal to 50 kHz and the ^{35}Cl carrier frequency was set at $\delta_{35Cl,1Q}$ = 130 ppm. The τ_{mix} delays were equal to 1280 or 1000 μs for T-HMQC and *D*-HMQC experiments, respectively.

NaH_2PO_4. We acquired the 1D and 2D ^{1}H-{^{23}Na} *D*-HMQC, *D*-HMQC-TONE$_2$ and T-HMQC$_p$ spectra of NaH_2PO_4 with τ_{RD} = 5 s ($T_{1,1H} \approx$ 80 s). For the T-HMQC$_p$ experiments, the rf-field on the ^{23}Na channel was equal to 80 kHz and the ^{23}Na carrier frequency was set at $\delta_{23Na,1Q}$ = -15 ppm. The τ_{mix} delays were equal to 600 or 512 μs for T-HMQC$_p$ and *D*-HMQC experiments, respectively.

The ^{1}H isotropic chemical shifts were referenced to tetramethylsilane (TMS) using the signal of the CH_2 group of adamantane at 1.85 ppm as a secondary reference. ^{23}Na and ^{35}Cl isotropic chemical shifts were indirectly referenced using the previously published relative NMR frequencies [33]. The number of scans, *NS*, the number of t_1 increments, N_1, and the total experimental time, T_{exp}, are given in the captions of Figs.**S3**, **S4** and **6**.

IV.2. ^{1}H-{^{35}Cl} HMQC spectra

To measure the resolution enhancement provided by the T-HMQC$_3$ experiment with respect to *D*-HMQC, we recorded the 2D ^{1}H-{^{35}Cl} *D*- and T-HMQC$_p$ spectra of histidine and cysteine. ^{35}Cl is a spin-3/2 isotope with high natural abundance, *NA* = 75.8 %, but a low gyromagnetic ratio: $\gamma_{35Cl}/\gamma_{1H} \approx$ 0.098. The simulations of 1D ^{35}Cl CPMG spectra of pure histidine and cysteine powders (Fig.**S2b**) yield the best-fit NMR parameters: (δ_{iso} (ppm), C_Q (MHz), η_Q) = (34, 1.95, 0.66) and (69, 4.78, 0.43), respectively.

As seen in Figs.**S3a** and **S4a**, the 2D *D*-HMQC spectra of these compounds exhibit a significant t_1-noise owing to the instabilities of the MAS frequency. Conversely, the 2D T-HMQC$_p$ spectra shown in Figs.**S3b-d** and **S4b-d** are free from t_1-noise.

The 2D T-HMQC$_1$ spectra shown in Fig.**S3b** and **S4b** are difficult to analyze, even for these samples containing a single ^{35}Cl species since each ^{35}Cl nucleus yields three distinct resonances along the ^{35}Cl axis: the 1Q-CT and 1Q-ST at the positions described in Table 1, and the 3Q one at a position that depends on the carrier frequency, owing to the 90° phase increment used in the States-TPPI procedure. Advantageously, the 2D T-HMQC$_2$ and T-HMQC$_3$ spectra (shown in Figs.**S3c** and **S3d** for histidine and Figs.**S4c** and **S4d** for cysteine) are simpler since each ^{35}Cl species only results in a single resonance, i.e. that related to 2Q coherences for the former experiment and 3Q for the latter.

Figs.**4a** and **4b** show a comparison using the $\delta_{35Cl,pQ}$ (ppm) scales of the 1D ^{35}Cl CPMG spectra of histidine and cysteine along with the sum projections onto the ^{35}Cl dimension of their 2D ^{1}H-{^{35}Cl} *D*- and T-HMQC$_p$ spectra. As rotor-synchronized t_1-increments, $\Delta t_1 = T_R$, were used for all 2D experiments, the spectral width along the indirect dimension, SW_1, in $\delta_{35Cl,pQ}$ (ppm) scale is inversely proportional to the p value and equal to 800 ppm = ν_R/ν_{0I} for *D*-HMQC and T-HMQC$_1$, 400 ppm = $\nu_R/(2\nu_{0I})$ for T-HMQC$_2$ and 267 ppm = $\nu_R/(3\nu_{0I})$ for T-HMQC$_3$ experiments. The vertical red lines indicate the position

of the isotropic chemical shifts, δ_{iso}. The resonance frequencies of the various coherences are consistent with the QIS values given in Table 1. In particular, the center of gravity of the 3Q resonance is symmetrical of that of the 1Q-CT with respect to δ_{iso}. According to the linewidth values given in Table 1, the 2Q resonances displayed in the $\delta_{35Cl,2Q}$ scale should be 18 times narrower than the 1Q-CT ones. However, this is not the case, especially for histidine, for which the experimental linewidths of 1Q-CT and 2Q resonances are similar (Fig.**4a**). The additional experimental broadening of the 2Q resonance may originate from a residual first-order quadrupolar interaction not perfectly canceled owing to spinning speed fluctuations and/or misadjustment of the magic angle. It may also originate from a short T_2' value for these coherences that are subject to first-order quadrupolar interactions. However, it must be noted that such broadening is not observed with cysteine, for which the local environment of ^{35}Cl nuclei is close to that of histidine. This extra-broadening in the case of histidine leads to an overlap of the 2Q resonance with the red line corresponding to δ_{iso}. Advantageously, the 3Q coherences are not affected by the first-order quadrupolar interaction and hence, these resonances are always narrower than the 1Q-CT ones, in agreement with the theoretical linewidths given in Table 1. It must be noted that the line-widths of the 3Q resonances in Figs.**S3b** and **S4b** look three-times broader than those in Figs.**S3d** and **S4d**; this is related to the factor of 3 used for the $\delta_{35Cl,3Q}$ ppm scaling.

We tried to record the 2D ^{1}H-{^{35}Cl} *D*- and T-HMQC$_p$ spectra of a physical mixture of histidine and cysteine. However, these two samples reacted in the rotor under MAS condition and the acquired 2D spectra were evolving in the course of the acquisition. To circumvent this issue, we summed the 2D spectra of the two pure compounds, which would correspond to a hypothetical physical mixture with molar ratios equal to that of the number of transients acquired for each sample.

Figs.**4c** and **S5** illustrate in the case of this hypothetical mixture a significant resolution improvement for T-HMQC$_2$ and T-HMQC$_3$ spectra with respect to *D*-HMQC and T-HMQC$_1$. Furthermore, the T-HMQC$_3$ method has the advantage that it does not require STMAS conditions to enhance the resolution. We can also notice that the resolution enhancement in $\delta_{35Cl,3Q}$ (ppm) is larger than the 27/7 theoretical value predicted from the ratio of linewidths given in Table 1. This higher resolution gain results from the fact that the cysteine resonance with δ_{iso} = 69 ppm, exhibits a higher QIS = 98.6 ppm than the histidine resonance with δ_{iso} = 34 ppm and QIS = 17.7 ppm. As a result, the gravity centers of the resonances are located at 16.3 (34 - 17.7) and -29.6 (69 - 98.6) or 51.7 (34 + 17.7) and 167.6 (69 + 98.6) ppm for histidine and cysteine, with *D*-HMQC or T-HMQC$_3$, leading to a separation of the two resonances equal to 45.9 or 115.9 ppm, respectively. Therefore, in this particular case, the experimental resolution gain is equal to 9.7 (27/7×115.9/45.9).

IV.3. ^{1}H-{^{23}Na} *D*- and T-HMQC spectra

The comparison of the ^{1}H-{^{35}Cl} *D*- and T-HMQC spectra has demonstrated how the T-HMQC$_3$ sequence enhances the resolution and limits the t_1-noise, as seen in Figs.**4** and **S3**-**S5**. We have then compared the sensitivity of the T-HMQC$_3$, *D*-HMQC and *D*-HMQC-TONE$_2$ experiments for the indirect detection of ^{23}Na nuclei via protons in NaH_2PO_4, which contains four crystallographically inequivalent ^{1}H sites (denoted H_1 to H_4) with δ_{iso} = 11.1, 9.3, 12.4 and 12.8 ppm [34] and two distinct ^{23}Na sites with (δ_{iso} (ppm), C_Q (MHz), η_Q) = (-2.5, 1.6, 0.5) for Na_1 and (-6.4, 2.35, 1.0) for Na_2, corresponding at B_0 = 9.4 T to $QIS_{1Q\text{-}CT}$ = -6.2 and -16.4 ppm and $\langle H_{Q2}\rangle_{1Q\text{-}CT}$ = 14.4 and 36 ppm, respectively [35,36]. The neutron diffraction analysis has revealed that the shortest Na-H distances range from 270 to 280 pm, which result in ^{1}H-^{23}Na dipolar coupling constants, $|b_{1H\text{-}23Na}|/(2\pi) \approx 1.6$ kHz [37].

Fig.**5** shows the 1D ^{1}H sum projections (corresponding to t_1 = 0) of the ^{1}H-{^{23}Na} *D*- and T-HMQC spectra of NaH_2PO_4, acquired at B_0 = 9.4 T ($\nu_{0,23Na}$ = 105.8 MHz) with ν_R = 62.5 kHz and $\nu_{1,23Na}$ = 80 kHz for T-HMQC$_p$. These spectra differ mainly by their relative intensities. In spite of a larger number of pulses (compare Figs.**1b** and **1c**), the *D*-HMQC-TONE$_2$ spectrum is slightly more intense (1.05) than that of the conventional *D*-HMQC experiment since the additional pulses refocus the evolution under ^{1}H CSA and ^{1}H-^{1}H dipolar interactions. We can also notice that the intensities of the 1D T-HMQC spectra are roughly proportional to the number of coherences selected during the t_1 period: four for T-HMQC$_1$ (1Q-CT, two 1Q-ST and 3Q), two 2Q for T-HMQC$_2$ and one 3Q for T-HMQC$_3$ with an intensity of 2.71, 1.21 and 0.78, and hence, a contribution of each coherence equal to 0.68, 0.61 and 0.78, respectively. This result is in line with previous measurements (Fig.**18** of ref. [8]) and confirms that the TRAPDOR pulse distributes equally the population among the various coherences. The intensity

of the *D*-HMQC spectra is higher than that of T-HMQC$_3$ since the *D*-HMQC sequence employs CT-selective pulses, which selectively convert the populations of the energy levels ±1/2 into 1Q-CT coherences. Therefore, the intensity of the *D*-HMQC spectra is proportional to 1/2, whereas that related to one coherence in T-HMQC experiments of spin-3/2 is proportional to (3/2 + 1/2)/6 = 1/3, assuming that the TRAPDOR pulse distributes equally the populations among the various coherences. As a result, the relative intensity of the T-HMQC$_3$ experiment, which selects a single coherence of spin-3/2, is approximately 2/3 = 0.67 with respect to that of the *D*-HMQC.

Besides the signal intensity, the *D*- and T-HMQC sequences also differ by the signal-to-noise ratios, SNR, and sensitivities (S = SNR/$\sqrt{T_{exp}}$). To compare these ratios, we have recorded the 2D ^{1}H-{^{23}Na} *D*-HMQC, *D*-HMQC-TONE$_2$ and T-HMQC$_3$ spectra of NaH_2PO_4, with the same experimental time, $T_{exp} \approx 23$ h.

As expected, even if the conventional *D*-HMQC and its TONE$_2$ variant exhibit similar signal intensities, as seen in Fig.**5**, the later benefits from a reduced t_1-noise (compare Figs.**6a** and **6b**) and hence a higher SNR, even in this case where: (i) the ^{23}Na natural abundance is 100 %, which limits the amount of uncorrelated ^{1}H magnetization, (ii) the ^{1}H CSA is limited at 9.4 T, (iii) the sample rotation was stable, and (iv) the recovery delay, τ_{RD} = 5 s, was much shorter than $T_{1,1H} \approx 80$ s [6]. The gain in SNR (1.73 for $H_{3,4}$, 1.25 for H_1 and 1.39 for H_2) increases with ^{1}H CSA since the reduced anisotropy ($\delta_{zz} - \delta_{iso}$) [38,39] (with δ_{zz} the principal component of the CSA tensor farthest from δ_{iso}) of $H_{3,4}$, H_1 and H_2 are equal to 24.6, 23.4, 20.2 and 22.7 ppm for H_4, H_3, H_1 and H_2 [35].

The 2D ^{1}H-{^{23}Na} T-HMQC$_3$ spectrum of NaH_2PO_4 sample is shown in Fig.**6c**. Since the line-width in Hz of the 3Q resonance is 7/9 that of 1Q-CT, a fair comparison of the 2D spectra requires to sample longer the t_1 period by 9/7 for T-HMQC$_3$ compared with *D*-HMQC and *D*-HMQC-TONE$_2$ experiments. In agreement with Table 1, the resonance frequencies of 3Q and 1Q-CT coherences are symmetrical with respect to δ_{iso}, and the 3Q resonances are about 27/7 ≈ 3.9 times narrower than the 1Q-CT ones using the $\delta_{23Na,3Q}$ (ppm) scale. Nevertheless, as the Na_1 deshielded resonance at δ_{iso} = -2.5 ppm exhibits a smaller QIS = 6.2 ppm than the Na_2 shielded one with δ_{iso} = -6.4 ppm and QIS = 16.4 ppm, the 3Q resonances of NaH_2PO_4 are separated by 6.3 ppm {(6.4 + 16.4) - (-2.5 + 6.2)}, instead of 14.1 ppm {(-2.5 - 6.2) - (-6.4 - 16.4)}. Therefore, the overall resolution improvement is equal to 1.7 = 27/7×6.3/14.1. As a result, the two ^{23}Na resonances overlap because the half-sum of their widths, {$\langle H_{Q2}\rangle_{Na1}$ + $\langle H_{Q2}\rangle_{Na2}$}/2, is larger than their separation: 25.2 > 14.1 and 6.5 > 6.3 ppm for both *D*- and T-HMQC$_3$ spectra, respectively.

The *D*-HMQC-TONE$_2$ and T-HMQC$_3$ sequences exhibit reduced t_1-noise, which is below the thermal noise in Fig.**6b** and **6c**. The number of acquisitions ($NS \times N_1$) being the same, these two spectra have the same noise. The integrated signal intensities are proportional to the product of *NS* and the transfer efficiencies shown in Fig.**5**, but the maximum signal amplitudes are inversely proportional to the linewidths of the resonances ($\langle H_{Q2}\rangle$ in Table 1). So, globally the SNR of the resonances shown in Fig.**6b** and **6c** are approximately proportional to the transfer efficiencies shown in Fig.**5**: (190, 116, 111) and (135, 88, 82) for *D*-HMQC-TONE$_2$ and T-HMQC$_3$, for $H_{3,4}$, H_1 and H_2, respectively. It is important to note that these large SNRs of T-HMQC have been obtained because we used a large rf-field of $\nu_{1,23Na}$ = 80 kHz, but using a large rf-field may be a limitation in the case of low-gamma nuclei. Conversely, the *D*-HMQC-TONE$_2$ sequence does not require a large rf-field because it only applies CT-selective pulses to the quadrupolar nuclei.

V. Conclusions

We have compared the conventional *D*-HMQC sequence and its TONE$_2$ variant. We have shown that the second sequence should be preferred because it leads to a slightly higher signal and a much larger SNR due to strongly reduced t_1-noise [4].

We have demonstrated how the 2D T-HMQC$_3$ method using a six-step phase cycle can improve the resolution for the NMR observation in crystalline samples of spin-3/2 nuclei, such as ^{23}Na and ^{35}Cl, with respect to 1D spectra and 2D *D*-HMQC experiments. The gain in resolution stems from the three-fold

increase in resonance frequencies of 3Q coherences with respect to 1Q ones, as well as the smaller second-order quadrupolar broadening (7/9 in Hz) of the 3Q resonances compared to 1Q-CT. Furthermore, the 3Q coherences are not affected by the first-order quadrupolar interaction and hence, the T-HMQC$_3$ method is robust to MAS frequency instabilities and maladjustment of the magic angle. This contrasts with the T-HMQC$_2$ variant, which selects the 2Q resonances that are subject to the first-order quadrupolar interaction. When the quadrupolar parameters of all species are identical, the resolution gain is close to 4. However, the QIS and hence, the separation between the resonances depend on the analyzed coherences. Therefore, the actual gain in resolution between T-HMQC$_3$ and *D*-HMQC depends on the isotropic chemical shifts and the quadrupolar parameters. For instance, we measured a resolution improvement of 9.7 for the ^{1}H-{^{35}Cl} T-HMQC$_3$ spectrum of a hypothetical mixture of L-histidine·HCl and L-cysteine·HCl, but only 1.7 for the ^{1}H-{^{23}Na} T-HMQC$_3$ spectrum of NaH_2PO_4. In the case of samples presenting distributions of isotropic chemical shifts, the resolution gain would be smaller. In any case, the two methods, *D*-HMQC-TONE and T-HMQC$_3$ are complementary for spin-3/2 nuclei, because they provide different spectral information.

The 3Q coherences in T-HMQC$_3$ experiments are efficiently created by the TRAPDOR pulses, which distribute the populations in the different coherences of the spin-3/2 density matrix. Numerical simulations show that in general the TRAPDOR pulses must employ large rf-fields equal to the maximum value compatible with the rf-power specification of the MAS probe, in order to maximize the transfer efficiency and to reduce the recoupling time and hence, the losses associated to ^{1}H-^{1}H dipolar interactions. Furthermore, the T-HMQC$_3$ sequence is robust to offset owing to the contribution of high-order cross-terms between heteronuclear dipolar interaction and rf-field, except that the carrier frequency of the TRAPDOR pulse must not be resonant with the spin-3/2 signals. Hence, the T-HMQC$_3$ sequence only requires the optimization of a single parameter, the length of the TRAPDOR pulses.

The analysis of the ^{1}H-{^{35}Cl} *D*-HMQC-TONE$_2$ and T-HMQC$_3$ spectra confirms that the two sequences lead to a negligible t_1-noise. ^{1}H-{^{23}Na} experiments on NaH_2PO_4 show that the transfer efficiency of T-HMQC$_3$ with 80 kHz rf-field is about 25 % lower than that of *D*-HMQC-TONE$_2$. Hence, the T-HMQC$_3$ experiment yields higher resolution with respect to D-HMQC-TONE, but at the expense of lower sensitivity.

Furthermore, it must be noted that the indirect spectral-width of the rotor-synchronized T-HMQC$_3$ experiments ($\Delta t_1 = T_R$) is three-fold lower than that of the *D*-HMQC experiments. In the case of insufficient indirect spectral-width, a non-rotor-synchronized acquisition ($\Delta t_1 < T_R$) can be used because 3Q coherences are not subject to first-order quadrupolar interactions.

It is preferable to carry out T-HMQC experiments with high spinning speed, since (i) it increases the indirect spectral-width in the case of rotor-synchronized acquisition, (ii) the ^{1}H T_2' values are proportional to ν_R and hence, the losses decrease at high MAS frequency, (iii) a low diameter coil allows the use of higher rf-field, which shortens the recoupling time, and hence the losses, and (iv) high MAS frequencies enhance the ^{1}H resolution. Moreover, even at high-spinning speed, it has been shown that the ^{1}H resolution can still be enhanced using homonuclear decoupling schemes [40-42].

A practical difficulty for the use of the T-HMQC$_3$ sequence is that the indirect frequency dimension must be scaled down by a factor 3 to facilitate the comparison with the 1D spectra and the 2D *D*-HMQC sequences. This data treatment may not be easy to perform on some consoles, and hence, we provide an AU program in the SI, which allows doing it with the Bruker Topspin software. It must be noted that with spin-3/2 nuclei, the same resolution enhancement by a factor of ca. 4 may be obtained with the *D*-HMQC sequence by adding to each CT-selective $\pi/2$-pulse an off-resonance cosine modulation to perform the 1Q-CT $\leftrightarrow$ 3Q transfers [43]. However, this sequence does not reduce the t_1-noise.

Acknowledgments. Chevreul Institute (FR 2638), Ministère de l'Enseignement Supérieur, de la Recherche et de l'Innovation, Hauts-de-France Region, and FEDER are acknowledged for supporting and funding partially this work. Financial support from the IR-RMN-THC FR-3050 CNRS for conducting the research is gratefully acknowledged. OL and RB acknowledges financial support contract ANR-18-CE08-0015-01 (ThinGlass) and T-UEPEARL-20-005-LAFON-HAMDOUNA (NMR-MECA-DRUG). IH and ZG acknowledge the support by the National Science Foundation through NSF/DMR-1644779 and the State of Florida to the National High Magnetic Field Laboratory.

[1] S.E. Ashbrook, S. Sneddon, New Methods and Applications in Solid-State NMR Spectroscopy of Quadrupolar Nuclei, *J. Am. Chem. Soc.* 136 (**2014**) 15440–15456. https://doi.org/10.1021/ja504734p.

[2] M.K. Pandey, H. Kato, Y. Ishii, Y. Nishiyama, Two-dimensional proton-detected ^{35}Cl/^{1}H correlation solid-state NMR experiment under fast magic angle sample spinning: application to pharmaceutical compounds, *Phys. Chem. Chem. Phys.* 18 (**2016**) 6209–6216. https://doi.org/10.1039/C5CP06042G.

[3] A. Venkatesh, M.P. Hanrahan, A.J. Rossini, Proton detection of MAS solid-state NMR spectra of half-integer quadrupolar nuclei, *Solid State Nuclear Magnetic Resonance*. 84 (**2017**) 171–181. https://doi.org/10.1016/j.ssnmr.2017.03.005.

[4] A. Venkatesh, X. Luan, F.A. Perras, I. Hung, W. Huang, A.J. Rossini, t_1-Noise eliminated dipolar heteronuclear multiple-quantum coherence solid-state NMR spectroscopy, *Phys. Chem. Chem. Phys.* 22 (**2020**) 20815–20828. https://doi.org/10.1039/D0CP03511D.

[5] F.A. Perras, T.W. Goh, W. Huang, t_1-noise elimination by continuous chemical shift anisotropy refocusing, *Solid State Nuclear Magnetic Resonance*. 120 **(2022**) 101807. https://doi.org/10.1016/j.ssnmr.2022.101807.

[6] F.A. Perras, M. Pruski, Reducing t_1 noise through rapid scanning, *J. Mag. Res.* 298 (**2019**) 31–34. https://doi.org/10.1016/j.jmr.2018.11.008.

[7] I. Hung, Z. Gan, High-Resolution NMR of S = 3/2 Quadrupole Nuclei by Detection of Double-Quantum Satellite Transitions via Protons, *J. Phys. Chem. Lett*. (**2020**) 4734–4740. https://doi.org/10.1021/acs.jpclett.0c01236.

[8] R. Bayzou, J. Trébosc, I. Hung, Z. Gan, O. Lafon, J.-P. Amoureux, Indirect NMR detection via proton of nuclei subject to large anisotropic interactions, such as ^{14}N, ^{195}Pt, and ^{35}Cl, using the T-HMQC sequence, J. Chem. Phys. 156 (**2022**) 064202. https://doi.org/10.1063/5.0082700.

[9] J.A. Jarvis, I.M. Haies, P.T.F. Williamson, M. Carravetta, An efficient NMR method for the characterisation of ^{14}N sites through indirect ^{13}C detection., *Phys. Chem. Chem. Phys*. 15 (**2013**) 7613–7620. https://doi.org/10.1039/c3cp50787d.

[10] J.A. Jarvis, I. Haies, M. Lelli, A.J. Rossini, I. Kuprov, M. Carravetta, P.T.F. Williamson, Measurement of ^{14}N quadrupole couplings in biomolecular solids using indirect-detection ^{14}N solid-state NMR with DNP, *Chem. Commun*. 53 (**2017**) 12116–12119. https://doi.org/10.1039/C7CC03462H.

[11] J.A. Jarvis, M. Concistre, I.M. Haies, R.W. Bounds, I. Kuprov, M. Carravetta, P.T.F. Williamson, Quantitative analysis of ^{14}N quadrupolar coupling using ^{1}H detected ^{14}N solid-state NMR, *Phys. Chem. Chem. Phys.* 21 (**2019**) 5941–5949. https://doi.org/10.1039/C8CP06276E.

[12] S.E. Ashbrook, S. Wimperis, High-resolution NMR of quadrupolar nuclei in solids: the satellite-transition magic angle spinning (STMAS) experiment, *Progress in Nuclear Magnetic Resonance Spectroscopy*. 45 (**2004**) 53–108. https://doi.org/10.1016/j.pnmrs.2004.04.002.

[13] A. Brinkmann, A.P.M. Kentgens, Proton-Selective ^{17}O-^{1}H Distance Measurements in Fast Magic-Angle-Spinning Solid-State NMR Spectroscopy for the Determination of Hydrogen Bond Lengths, *J. Am. Chem. Soc.* 128 (**2006**) 14758–14759.

[14] P. Caravatti, G. Bodenhausen, R.R. Ernst, Selective Pulse Experiments in High-Resolution Solid State NMR, J*. Magn. Reson*. 55 (**1983**) 88–103.

[15] A.J. Pell, K.J. Sanders, S. Wegner, G. Pintacuda, C.P. Grey, Low-power broadband solid-state MAS NMR of ^{14}N, *J. Chem. Phys*. 146 (**2017**) 194202. https://doi.org/10.1063/1.4983220.

[16] A.J. Vega, MAS NMR spin locking of half-integer quadrupolar nuclei, *J. Magn. Reson.* 96 **(1992**) 50–68. https://doi.org/10.1016/0022-2364(92)90287-H.

[17] G. Pileio, M. Concistrè, N. McLean, A. Gansmüller, R.C.D. Brown, M.H. Levitt, Analytical theory of gamma-encoded double-quantum recoupling sequences in solid-state nuclear magnetic resonance., *J. Magn. Res.* 186 (**2007**) 65–74. https://doi.org/10.1016/j.jmr.2007.01.009.

[18] C. Martineau, B. Bouchevreau, F. Taulelle, J. Trébosc, O. Lafon, J.-P. Amoureux, High-resolution through-space correlations between spin-1/2 and half-integer quadrupolar nuclei using the MQ-D-R-INEPT NMR experiment., *Phys. Chem. Chem*. *Phys.* 14 (**2012**) 7112–7119. https://doi.org/10.1039/c2cp40344g.

[19] J.-P. Amoureux, C. Huguenard, F. Engelke, F. Taulelle, Unified representation of MQMAS and STMAS NMR of half-integer quadrupolar nuclei, *Chem. Phys. Lett*. 356 (**2002**) 497–504. https://doi.org/10.1016/S0009-2614(02)00398-6.

[20] S.P. Brown, S. Wimperis, Two-Dimensional Multiple-Quantum MAS NMR of Quadrupolar Nuclei: A Comparison of Methods, *J. Magn. Reson.* 128 (**1997**) 42–61. https://doi.org/10.1006/jmre.1997.1217.

[21] D. Marion, M. Ikura, R. Tschudin, A. Bax, Rapid recording of 2D NMR spectra without phase cycling. Application to the study of hydrogen exchange in proteins, *J. Mag. Res.* 85 (**1989**) 393–399. https://doi.org/10.1016/0022-2364(89)90152-2.

[22] Z. Gan, Isotropic NMR Spectra of Half-Integer Quadrupolar Nuclei Using Satellite Transitions and Magic-Angle Spinning, *J. Am. Chem. Soc*. 122 (**2000**) 3242–3243. https://doi.org/10.1021/ja9939791.

[23] C. Huguenard, F. Taulelle, B. Knott, Z. Gan, Optimizing STMAS, *J. Mag. Res*. 156 (**2002**) 131–137. https://doi.org/10.1006/jmre.2002.2548.

[24] S.E. Ashbrook, S. Wimperis, Satellite-Transition MAS NMR of Spin I=3/2, 5/2, 7/2, and 9/2 Nuclei: Sensitivity, Resolution, and Practical Implementation, **J. Mag. Res**. 156 (**2002**) 269–281. https://doi.org/10.1006/jmre.2002.2557.

[25] J.-P. Amoureux, C. Fernandez, Triple, quintuple and higher order multiple quantum MAS NMR of quadrupolar nuclei., *Solid State Nuclear Magnetic Resonance*. 10 (**1998**) 211–23.

[26] J. Trébosc, J.-P. Amoureux, Z. Gan, Comparison of high-resolution solid-state NMR MQMAS and STMAS methods for half-integer quadrupolar nuclei, *Solid State Nuclear Magnetic Resonance*. 31 (**2007**) 1–9. https://doi.org/10.1016/j.ssnmr.2006.09.002.

[27] M. Bak, J.T. Rasmussen, N.C. Nielsen, SIMPSON: a general simulation program for solid-state NMR spectroscopy., *J. Mag. Res*. 147 (**2000**) 296–330. https://doi.org/10.1006/jmre.2000.2179.

[28] M. Bak, N.Chr. Nielsen, REPULSION, A Novel Approach to Efficient Powder Averaging in Solid-State NMR, *J. Mag. Res*. 125 (**1997**) 132–139.

[29] D.G. Cory, W.M. Ritchey, Suppression of signals from the probe in bloch decay spectra, *J. Magn. Reson*. 80 (**1988**) 128–132.

[30] M. Goswami, P.J.M. van Bentum, A.P.M. Kentgens, Sensitivity enhancement in MAS NMR of half-integer quadrupolar nuclei using sideband selective double-frequency sweeps, *Canadian Journal of Chemistry*. 89 (**2011**) 1130–1137. https://doi.org/10.1139/V11-053.

[31] F.H. Larsen, H.J. Jakobsen, P.D. Ellis, N.Chr. Nielsen, Sensitivity-Enhanced Quadrupolar-Echo NMR of Half-Integer Quadrupolar Nuclei. Magnitudes and Relative Orientation of Chemical Shielding and Quadrupolar Coupling Tensors, *J. Phys. Chem.* A. 101 (**1997**) 8597–8606.

[32] D. Massiot, F. Fayon, M. Capron, I. King, S. Le Calvé, B. Alonso, J.-O. Durand, B. Bujoli, Z. Gan, G. Hoatson, Modelling one- and two-dimensional solid-state NMR spectra, *Magn. Reson. Chem*. 40 (**2002**) 70–76.

[33] R.K. Harris, E.D. Becker, S.M. Cabral de Menezes, R. Goodfellow, P. Granger, NMR nomenclature . Nuclear spin properties and conventions for chemical shifts, *Pure and Applied Chemistry*. 73 (**2001**) 1795–1818.

[34] L. Mafra, J.R.B. Gomes, J. Trébosc, J. Rocha, J.-P. Amoureux, ^{1}H-^{1}H double-quantum CRAMPS NMR at very-fast MAS (ν_R=35 kHz): a resolution enhancement method to probe ^{1}H-^{1}H proximities in solids, *J. Magn. Res*. 196 (**2009**) 88–91. https://doi.org/10.1016/j.jmr.2008.10.009.

[35] O. Lafon, Q. Wang, B. Hu, F. Vasconcelos, J. Trébosc, S. Cristol, F. Deng, J.-P. Amoureux, Indirect Detection via Spin-1/2 Nuclei in Solid State NMR Spectroscopy: Application to the Observation of Proximities between Protons and Quadrupolar Nuclei, *J. Phys. Chem*. A. 113 (**2009**) 12864–12878. https://doi.org/10.1021/jp906099k.

[36] A. Sasaki, J. Trébosc, J.-P. Amoureux, Accelerating the acquisition of high-resolution quadrupolar MQ/ST-HETCOR 2D spectra under fast MAS via ^{1}H detection and through-space population transfers, *J. Magn. Reson*. 333 (**2021**) 107093. https://doi.org/10.1016/j.jmr.2021.107093.

[37] R.N.P. Choudhary, R.J. Nelmes, K.D. Rouse, A room-temperature neutron-diffraction study of NaH_2PO_4, *Chem. Phys. Lett.* 78 (**1981**) 102–105. https://doi.org/10.1016/0009-2614(81)85562-5.

[38] U. Haeberlen, High-Resolution NMR in Solids: Selective Averaging, Academic, New-York, **1976**.
[39] R.K. Harris, E.D. Becker, S.M. Cabral de Menezes, P. Granger, R.E. Hoffman, K.W. Zilm, Further conventions for NMR shielding and chemical shifts (IUPAC Recommendations 2008), *Pure and Applied Chemistry*. 80 (**2008**) 59–84. https://doi.org/10.1351/pac200880010059.
[40] M. Leskes, S. Steuernagel, D. Schneider, P.K. Madhu, S. Vega, Homonuclear dipolar decoupling at magic-angle spinning frequencies up to 65kHz in solid-state nuclear magnetic resonance, *Chem. Phys. Lett.* 466 (**2008**) 95–99. https://doi.org/10.1016/j.cplett.2008.10.029.
[41] Y. Nishiyama, X. Lu, J. Trébosc, O. Lafon, Z. Gan, P.K. Madhu, J.-P. Amoureux, Practical choice of ^{1}H-^{1}H decoupling schemes in through-bond ^{1}H-{X} HMQC experiments at ultra-fast MAS. *J. Magn. Reson.* 214 (**2012**) 151–158. https://doi.org/10.1016/j.jmr.2011.10.014.
[42] J. Tognetti, W.T. Franks, J.R. Lewandowski, S.P. Brown, Optimisation of ^{1}H PMLG homonuclear decoupling at 60 kHz MAS to enable ^{15}N–^{1}H through-bond heteronuclear correlation solid-state NMR spectroscopy, *Phys. Chem. Chem. Phys.* 24 (**2022**) 20258–20273. https://doi.org/10.1039/D2CP01041K.
[43] I. Hung, Z. Gan, On the use of single-frequency versus double-frequency satellite-transition pulses for MQMAS, *J. Magn. Reson*. 328 (**2021**) 106994. https://doi.org/10.1016/j.jmr.2021.106994.

Figure

Click here to access/download;Figure;221010 T-HMQC3 Figs.pdf

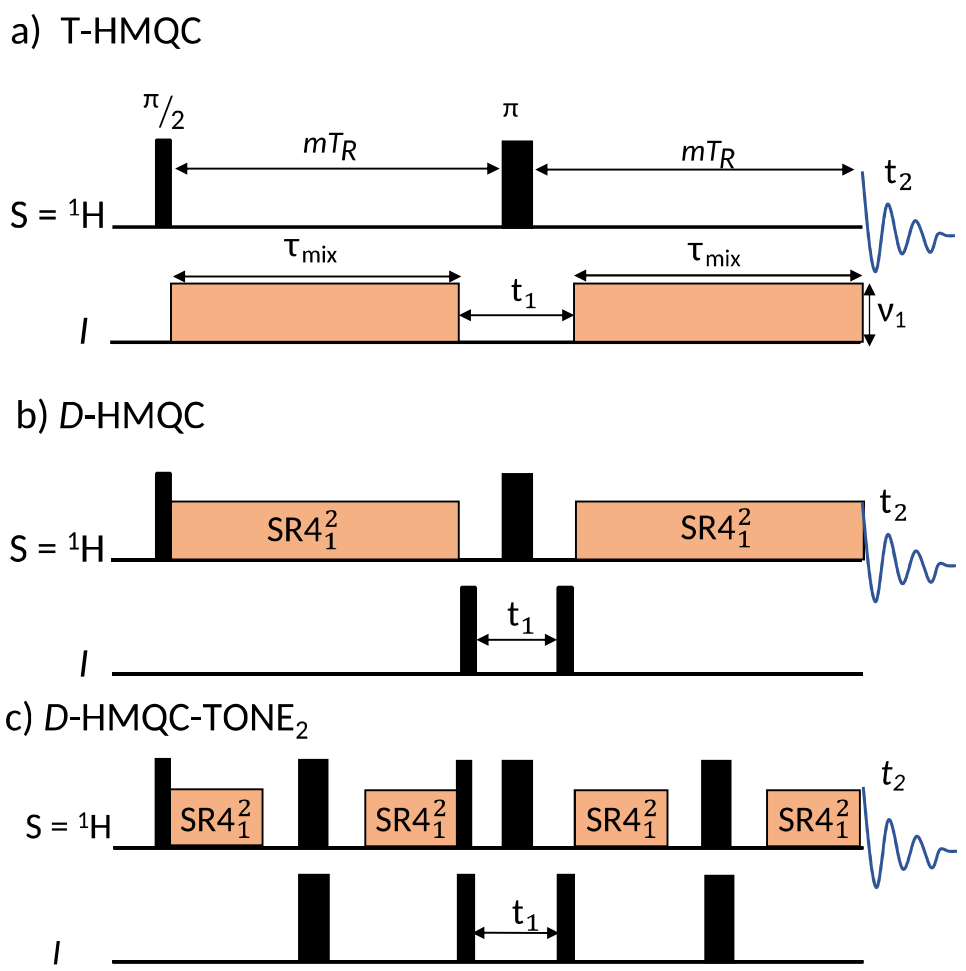

Fig.1. ^{1}H-{*I*} (a) T-HMQC, (b) *D*-HMQC, (c) *D*-HMQC-TONE$_2$ pulse sequences. ^{1}H-*I* dipolar couplings are reintroduced by applying the $SR4_1^2$ recoupling on the ^{1}H channel in the *D*-HMQC and *D*-HMQC-TONE$_2$ schemes or two identical long pulses on the *I* channel in the T-HMQC sequence. The narrow and wide black rectangles represent $\pi/2$ or π pulses, respectively. These pulses are selective of CT on the *I* channel.

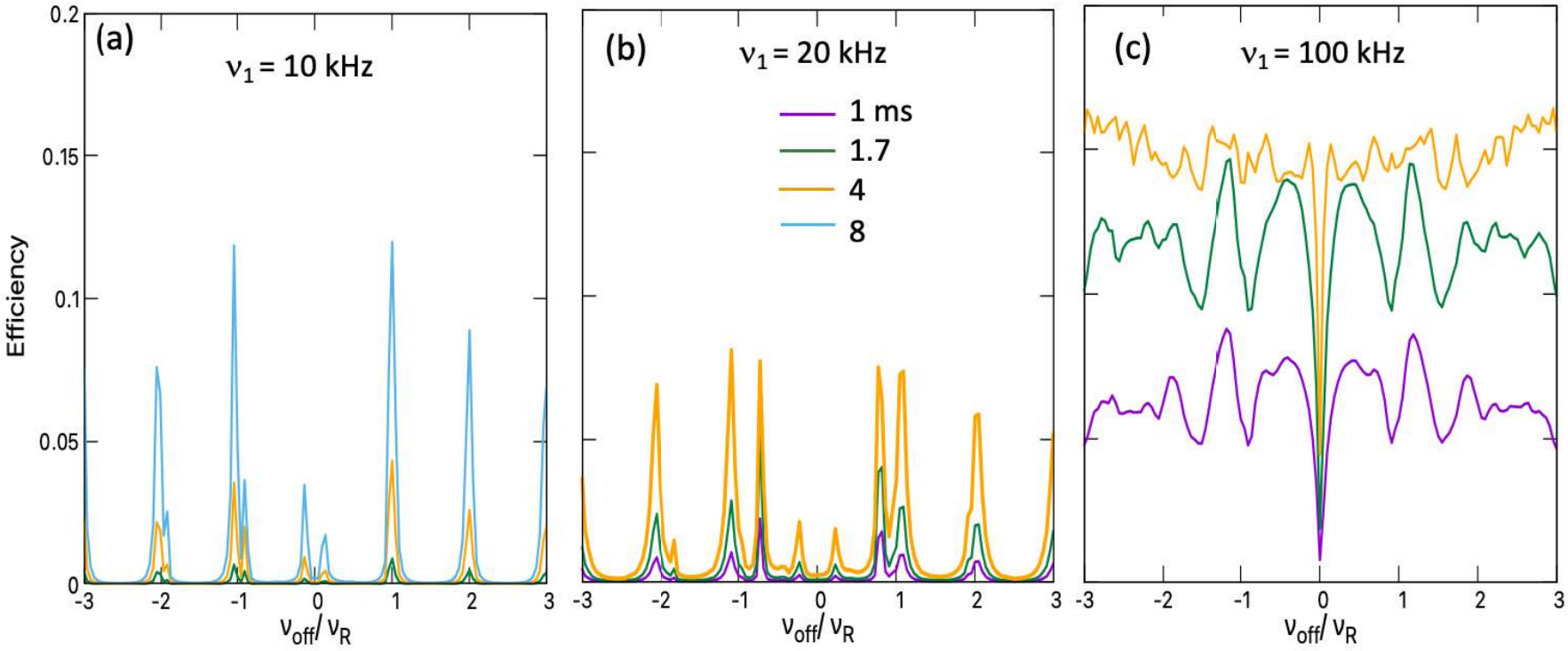

Fig.2. Simulations of the ^{1}H-{^{35}Cl} T-HMQC$_1$ (1Q-CT + 1Q-ST) efficiency versus the offset in reduced value, ν_{off}/ν_R, with B_0 = 18.8 T, ν_R = 62.5 kHz, C_Q = 1.95 MHz and η_Q = 0.66. ν_1 = 10 (a), 20 (b), and 100 (c) kHz. The τ_{mix} values are indicated with different colors.

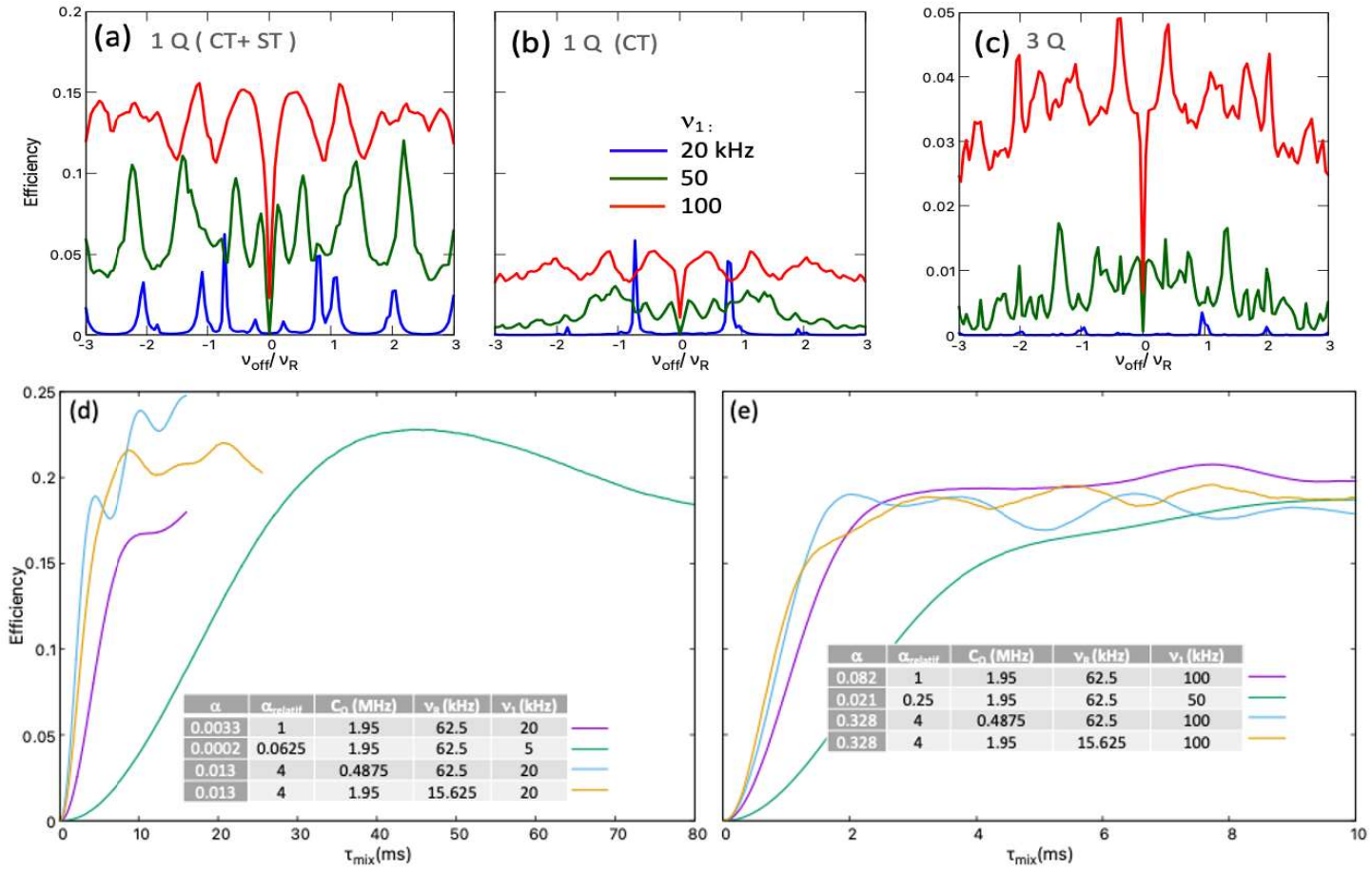

Fig.3. Simulations of the ^{1}H-{^{35}Cl} T-HMQC efficiency. (a-c) Versus offset with ν_1 = 20, 50, 100 kHz, and $\tau_{mix,opt}$ fixed according to each ν_1 value: (a) 1Q (CT + ST), (b) 1Q-CT and (c) 3Q. Note the fourfold lower efficiency scale in (c) with respect to (a) and (b). (d,e) Versus τ_{mix} with $\nu_{off} = \nu_R$ and either small (d) or large (e) rf-fields. The α, C_Q, ν_R and ν_1 values are indicated in the Tables. α_{rel} is the relative value with respect to the 1st line. The various sets of parameters are indicated with different colors.

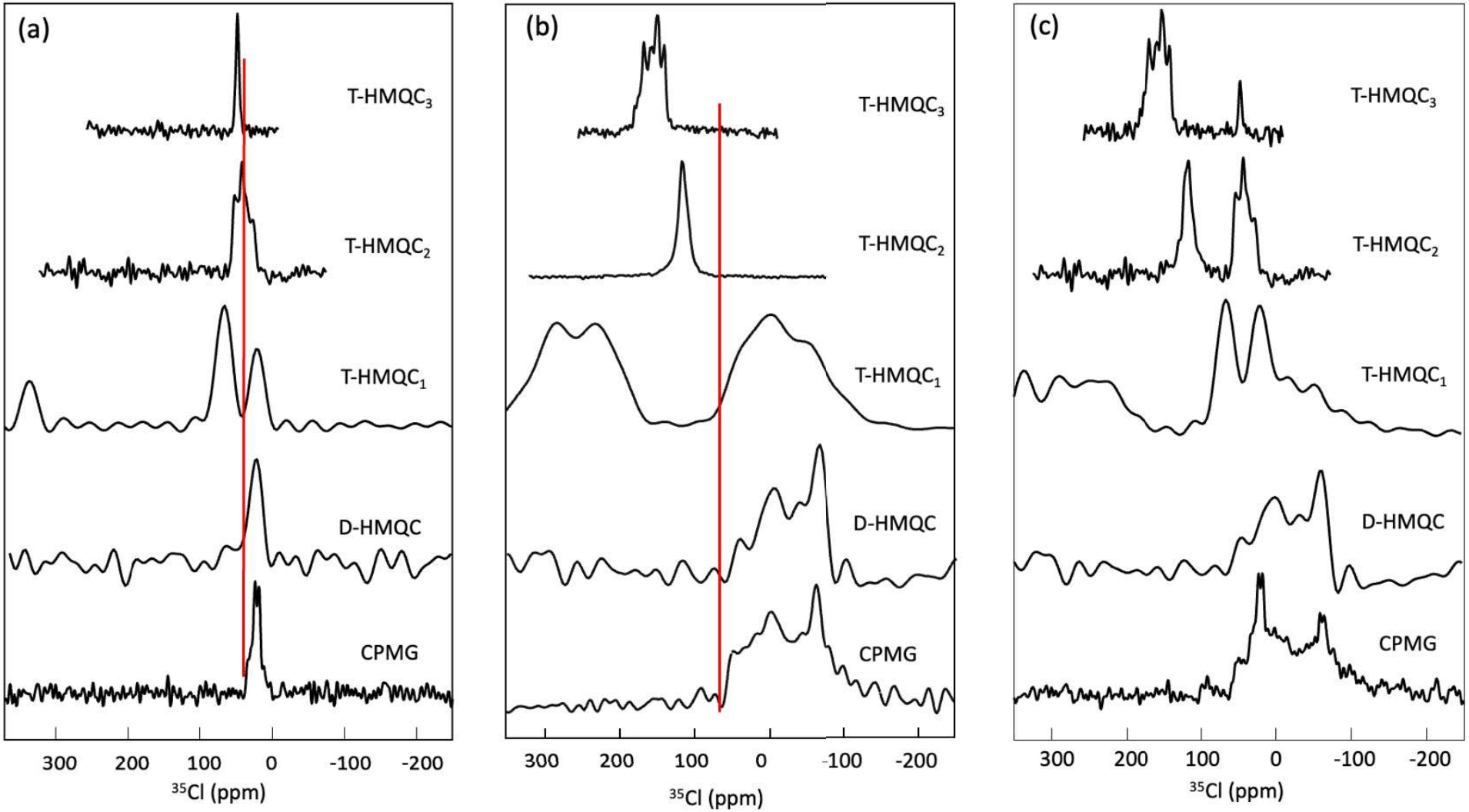

Fig.4. ^{35}Cl sum/projections of the 2D spectra (Fig.S3-S5) and CPMG 1D spectra of the pure (histidine and cysteine) and 'mixture' samples. The spectra are represented with the $\delta_{35Cl,pQ}$ ppm scales. (a,b) The isotropic chemical shifts are shown with the vertical red lines.

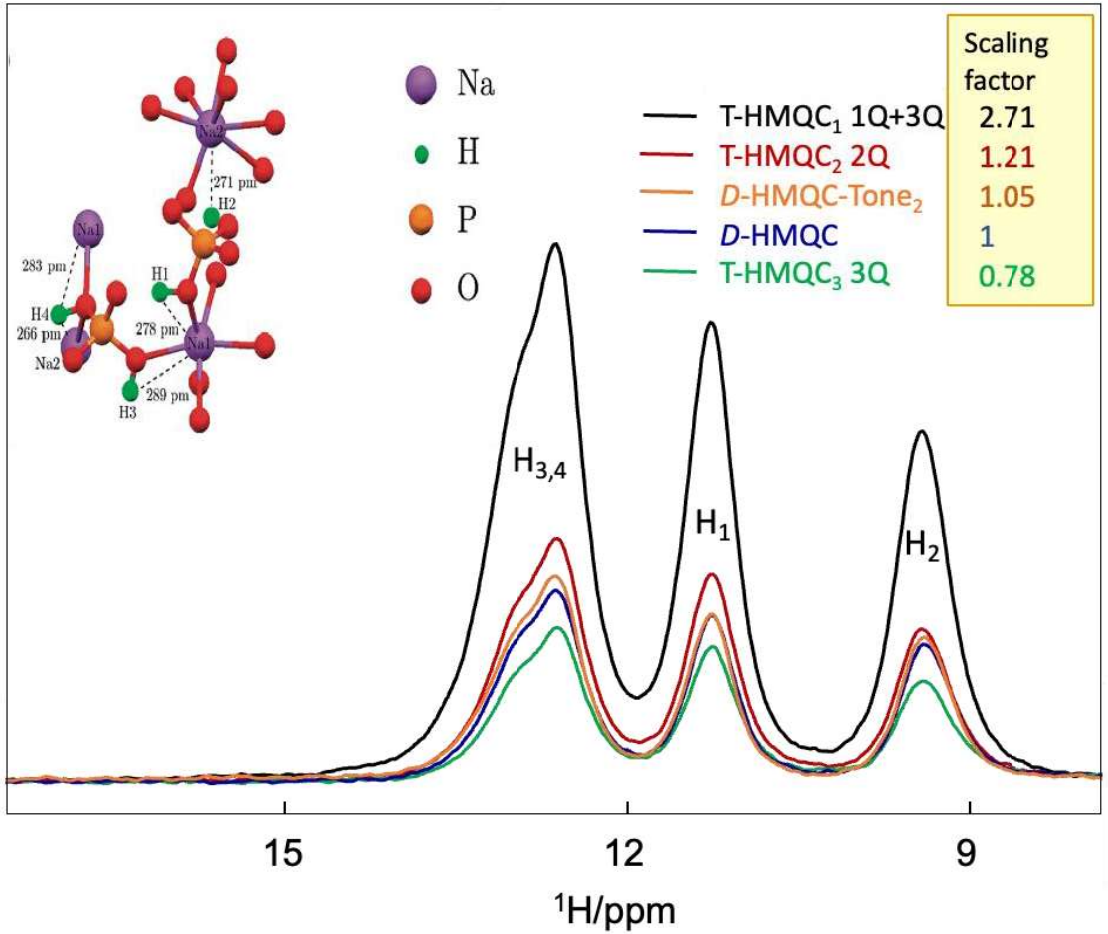

Fig.5. ^{1}H signal projections (t_1 = 0) of ^{1}H-{^{23}Na} HMQC spectra of NaH_2PO_4 (B_0 = 9.4 T, ν_R = 62.5 kHz, T_{exp} = 8 min) observed with *D*- or T-HMQC (ν_1 = 80 kHz) sequences. On the right of the figure, we give the scaling factors with respect to the conventional *D*-HMQC.

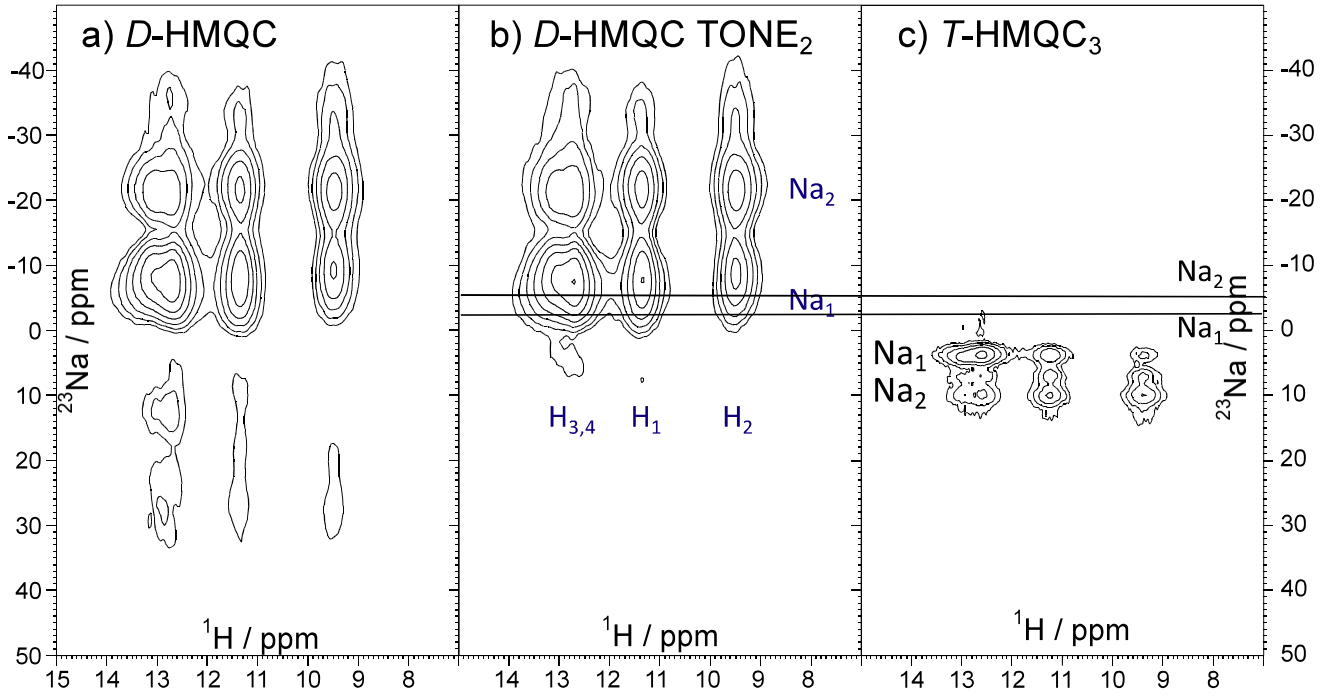

Fig.6. ^{1}H-{^{23}Na} 2D spectra of NaH_2PO_4 (B_0 = 9.4 T, ν_R = 62.5 kHz, $T_{exp} \approx$ 23 h). (a) *D*-HMQC (2 phases), (b) *D*-HMQC-Tone$_2$ (2 phases), (c) T-HMQC$_3$ (6 phases). (NS, N_1) = (128,128) (a), (128,128) (b), (96,164) (c). The ^{23}Na resonances observed in (a,b) are four times broader than those in (c) and symmetrical to them with respect to the horizontal red lines showing the isotropic chemical shifts.